An improved miniature mixed-mode delamination setup for in situ microscopic interface failure analyses

M Kolluri, J P M Hoefnagels, J a W van Dommelen, M G D Geers

An improved miniature mixed mode delamination setup for *in-situ* microscopic interface failure analyses

M Kolluri[2,1] J P M Hoefnagels[1], J A W van Dommelen[1] and M G D Geers[1]

[1] Department of Mechanical Engineering, Eindhoven University of Technology, P.O. Box 513, 5600 MB Eindhoven, The Netherlands

[2] Materials innovation institute (M2i), Mekelweg 2, P.O. Box 5008, 2600 GA Delft, The Netherlands

E-mail: j.p.m.hoefnagels@tue.nl

Abstract. Precise characterization of interface delamination in miniature interface structures is an ongoing challenge with the advent of miniaturization and multi-functionality in the electronics industry. Accurate numerical prediction of the interface behavior is necessary to minimize delamination failures. Successful prediction requires (i) accurate determination of the interface properties like the critical energy release rate, CERR, over the full range of mode mixities and (ii) simultaneous *in-situ* microscopic visualization of the delamination mechanism. These requirements were recently addressed by the development of the miniature mixed mode bending (MMMB) setup [Kolluri et al., Int. J. Frac. 2009]. In this article an improved MMMB setup is presented, which overcomes the main limitations of the original design. Specifically, the improved design (i) can access a significantly larger range of interface systems due to its increased limits of maximum accessible load and stroke in all mode mixities, (ii) has significantly higher accuracy in load-displacement measurement due to its reduced clearance at the connectors, which is particularly relevant for miniature samples, and (iii) has a high reproducibility due to a newly added setup alignment tool. The measurement concept is validated on (industrially relevant) copper lead frame-molding compound epoxy (CuLF-MCE) interface structures. The load-displacement curves and corresponding CERR values obtained from experiments over the full range of mode mixities are discussed in relation to the delamination mechanism observed during real-time *in-situ* visualization. Specifically, the measured increase of the CERR towards mode II is related to a more discrete or jerky crack growth behavior observed in the mode II dominant tests. Finally, the potential of the methodology for interface parameter characterization is illustrated.

1. Introduction

Interfacial delamination is a major concern in the micro-electronics industry (see, e.g. [1, 2] and Fig. 1(a,b)) due to the high density integration of dissimilar materials into a single so-called 'System in Package (SiP)', driven by ever-increasing demands for miniaturization and multi-functionality. Delamination occurs mainly due to significant thermal stresses generated at these interfaces during thermal cycling, triggered by the mismatch of the coefficient of thermal expansion (CTE) and the Poisson's ratio of the adherend layers. As a prime example, during encapsulation of SiPs with molding compound epoxy (MCE), interfaces between MCE and outer layers of the SiP are often susceptible to delamination (in particular lead frame-MCE and die-MCE interfaces, shown as dashed lines in Fig. 1(c)). Specifically, delamination of copper lead frame (CuLF)-MCE interfaces attracted significant attention from researchers [3–9]. Yet the behavior of this interface over the full range of mode mixities and the underlying delamination mechanism are still not well understood. One of the reasons for this is that under certain loading configurations interface delamination occurs in concurrence with plasticity in the bulk layers, which prevents accurate determination of representative Critical Energy Release Rate (CERR) values. Accurate prediction of the interface behavior in SiP manufacturing and exploitation is necessary to minimize these delamination failures and to improve design rules accordingly. Successful prediction of interfacial failure using available interface models [10–12], is only possible with the input of accurate and detailed measurements of the interface behavior obtained from well defined delamination experiments. To this end, this article presents a new improved Miniature Mixed Mode Bending (MMMB) delamination setup capable of measuring CERR values under simultaneous *in-situ* observation under the scanning electron microscope (SEM) or optical microscope. As an illustrative example, this setup is validated on measurements of the CERR of the CuLF-MCE interface for the full range of mode mixities.

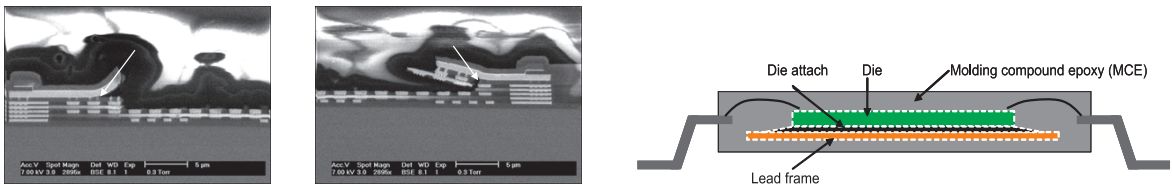

(a) (b) (c)

Figure 1. (a,b) SEM micrographs (arrows) showing delamination between copper metal lines and dielectric material in back end structures (Courtesy of NXP Semiconductors). (c) Schematic of the lead frame package molded in a molding compound epoxy. All the interfaces which are prone to delamination are marked as dashed lines.

It is well documented in the literature that interface fracture toughness is not a unique material property but depends on the entire stress field ahead of the crack

tip (i.e. loading mode) [13–19]. A complete description of an interface necessitates its characterization over the complete range of mode angles from mode I to mode II. Figure 2 shows the loading configurations typically used for testing under mode I (double cantilever beam (DCB) test, Fig. 2(a)) and mode II (end notch flexure (ENF) test, Fig. 2(b)). In contrast, Figure 2(c) shows the mixed mode bending test, which is capable of testing the full range of mode mixities. Besides controlling interface delamination under a well-defined mode angle in a single loading configuration, it is highly beneficial if the experimental methodology is able to carry out accurate *in-situ* delamination tests of miniature samples under optical and scanning electron microscopes. This enables to precisely identify the crack tip position and to understand the active delamination mechanism in addition to the CERR measurements. Due to the small forces involved with miniature samples, such a setup should not entail undesirable and non-negligible dissipative contributions due to friction and clearance in the moving parts of the setup that prohibit accurate force measurement. Furthermore, non-linearities resulting from the geometry of the setup and from the self weight of the parts of the setup should be avoided.

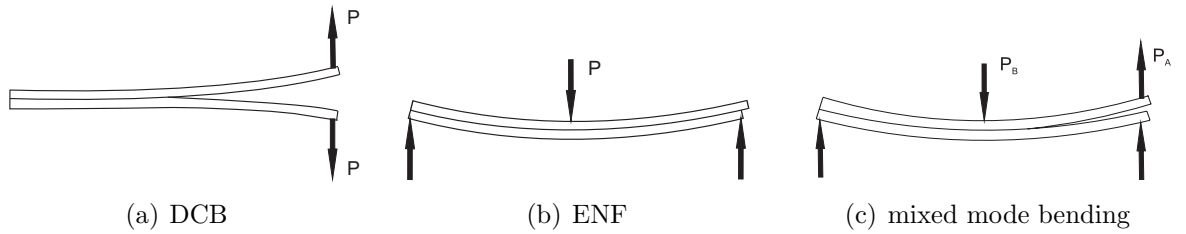

(a) DCB (b) ENF (c) mixed mode bending

Figure 2. Sketch of different loading configurations for interface delamination; (a) double cantilever beam (DCB) test; (b) end notch flexure (ENF) test; and (c) mixed mode bending test.

A number of experimental setups, which can carry out mixed mode delamination tests [7, 9, 16, 20–23], have been proposed in the literature. The setup of Reeder and Crews [20] is well known [9, 16, 24, 25] and can access a large range of mode mixities, however, excluding pure mode I and mode II. Hence, separate DCB tests and ENF tests are required to fulfill the interface characterization over the complete range of mode mixities [9]. Despite being suitable for mixed mode testing, none of the above mentioned setups are directly suitable for *in-situ* testing of miniature samples due to (i) their size being too large to handle miniature samples and to fit in a SEM chamber, (ii) their inability to keep the direction of load application horizontal, which is required to enable the use of standard microscopes to trace the crack tip movement and to visualize the delamination mechanism during *in-situ* testing, and (iii) the presence of friction resulting from moving hinges and parasitic non-linearities (e.g. through the self weight of the setup acting on the sample), which is especially a problem when testing miniature samples. To overcome these constraints, a redesigned miniature mixed mode bending (MMMB) setup was recently introduced by Kolluri et al. [26].

Proof of principle measurements on glued interfaces [26] indeed demonstrated that

the MMMB setup was successful in carrying out CERR measurements over the full range of mode mixities, under simultaneous *in-situ* microscopic visualization of the delamination mechanism. The remaining limitations of the setup proposed in [26] are (i) the maximum applied load (too limited) and (ii) maximum applied displacement (too small), (iii) instrumental hysteresis that required an elaborate digital image correlation procedure to correct for, and (iv) high operator skill to compensate lack of setup robustness and ease-of-use. Particularly, the first two limitations prevent testing of the industrially-relevant CuLF-MCE interfaces. This paper presents an improved miniature mixed mode bending delamination setup that overcomes the above-mentioned limitations, enabling a study on CuLF-MCE samples. First, a brief overview of the original MMMB design is given with its advantages and limitations. Next, the various improvements to the MMMB design are presented, and the design of the improved MMMB setup is confronted with the original MMMB setup. The functionality of the improved setup is demonstrated with tests on specially designed validation samples. Measurement accuracy and reproducibility are addressed by repeated tests on validation samples. Finally, the improved MMMB is used to study delamination in (preplated) CuLF-MCE samples over full range of mode mixities, and under *in-situ* SEM visualization of the delamination mechanism.

2. Brief review of the original MMMB setup

In this section, the main details of the loading configuration of the original MMMB design are reviewed [26]. The mixed mode bending loading configuration shown in figure 2(c) was adopted because of its ability to apply different mixed mode loading conditions and the fact that it is standardized (ASTM D6671-01, 2001, [27]), and widely accepted for interface delamination characterization. Figure 3 (left) shows the design of the original MMMB device to achieve the required mixed mode bending loading. The setup consists of several moving parts and special elastic hinges for frictionless rotation. The loads transferred to the sample, depicted in Fig. 3, can be written as:

$$P_A = P_{\mathrm{MMMB}}(1-\xi) \tag{1a}$$

$$P_B = P_{\mathrm{MMMB}}\frac{\alpha}{\beta}\xi \tag{1b}$$

$$P_C = \frac{P_B}{2} \tag{1c}$$

$$P_D = -P_A + \frac{P_B}{2}, \tag{1d}$$

where, $\xi = \frac{H}{\gamma}$ is a dimensionless shape parameter that represents the relative position of the applied load. H is the corresponding absolute position of the applied mixed mode load P_{MMMB} and α, β, γ are the characteristic dimensions of the loading mechanism (indicated in Fig. 3). Variation in the mode mixities is obtained by changing ξ over 13 discrete positions from 0 (DCB) to 1 (ENF).

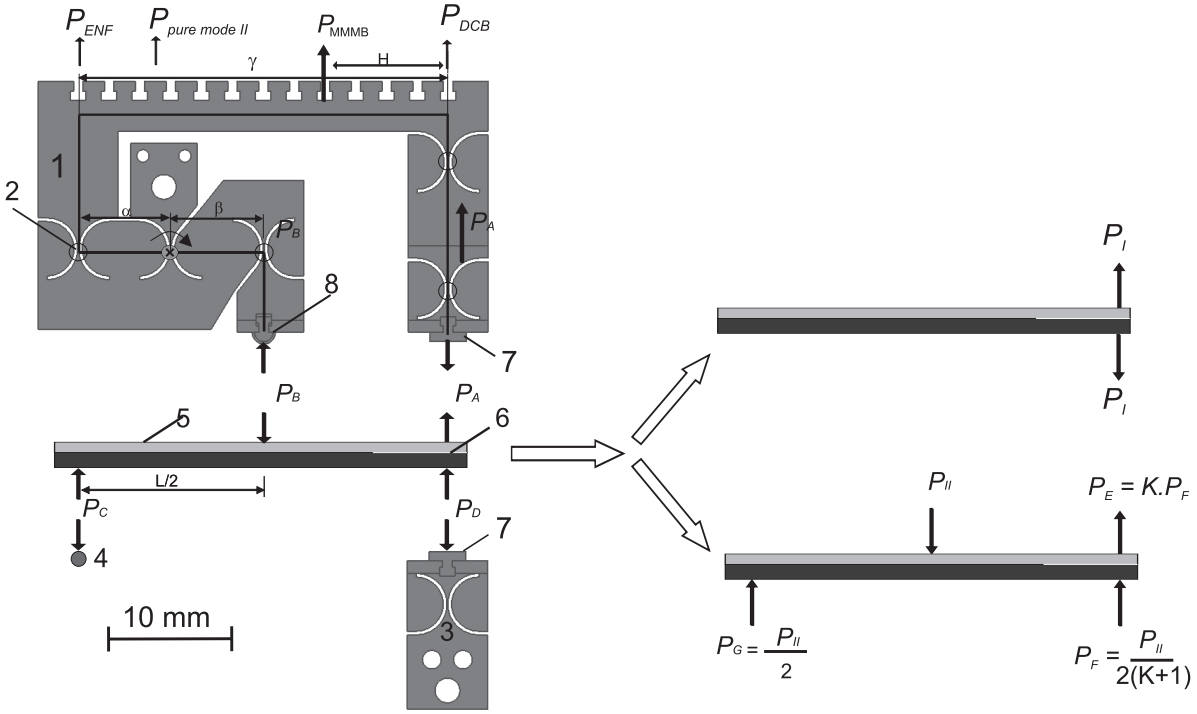

Figure 3. Design of the original MMMB device with: (1) the main loading mechanism (MLM) with (2) elastic hinges, (3) the bottom support hinge, (4) the left support, (5) the bilayer sample with (6) precrack, (7) the dovetail connector, and (8) loading tip. Also shown is the schematic representation of the load distribution under mixed mode bending, with the loads on the sample (shown on the left) and the decomposition of these loads into mode I and pure mode II components (shown on the right).

The load on the sample can be decomposed in its pure mode I and pure mode II components, P_I and P_{II}, respectively, which are defined by the load configurations depicted in the top and bottom right hand side of figure 3. Pure mode II loading is defined as the case for which the separating parts of the cracked specimen deform with the same curvature, resulting in a zero mode I component at the interface. The corresponding expressions for these mode I and mode II components in a bilayer sample with the same materials and equal layer thickness were presented previously [26]. Here, a more generalized form of these expressions for a bilayer sample with dissimilar materials and unequal layer thicknesses is presented. Details of the derivations are given in the appendix.

$$P_I = P_{\mathrm{MMMB}} \left(1 - \xi - \frac{K\alpha}{2\beta(1+K)} \xi \right), \tag{2}$$

$$P_{II} = P_{\mathrm{MMMB}} \frac{\alpha}{\beta} \xi, \tag{3}$$

where $K = \frac{P_E}{P_F}$ is a constant determined by the geometry and material properties of the two adherend dissimilar layers, which is equal to $K = \frac{E_t I_t}{E_b I_b}$ under the assumption of linear beam theory, with E_i and I_i the Young's modulus and moment of inertia for the

top and bottom layers respectively. It is clear from the Eqs. 2 and 3 that for $\xi = 0$, the applied loading corresponds to mode I (DCB) loading ($P_I = P_A = P_{\mathrm{MMMB}}$ and $P_{II} = 0$). For $\xi = 1$, the applied load corresponds to the conventional ENF loading ($P_{II} = P_B$ and $P_I = -P_{\mathrm{MMMB}}\frac{K\alpha}{2\beta(1+K)}$), where the presence of a negative mode I component leads to complications in the measurement of the mode II fracture toughness because of the friction between the two delaminated crack surfaces. For instance, results published by Kolluri et al. [26] showed a large difference in the CERR values obtained between pure mode II and ENF tests for glued interface samples. However, for any given bilayer sample, there is a position at which the mode I component is zero at the interface and consequently a pure mode II loading is obtained. This pure mode II loading position can be identified in this loading geometry by (see appendix)

$$\xi_{II} = \frac{2(1+K)\beta}{K\alpha + 2(1+K)\beta}. \tag{4}$$

The pure mode II position is $\xi = 0.8$ for the case of a homogeneous bilayer sample with equal thickness of the bulk layers and a setup with $\alpha = \beta$.

2.1. Advantages of the MMMB setup

The following reported advantages of the original MMMB setup are recalled: (i) delamination can be tested over the full range of mode mixities, (ii) precise force measurement for small samples during delamination, (iii) *in-situ* testing under optical or electron microscope is possible which enables identification of the precise crack tip position and delamination mechanisms, and (iv) frictionless pure mode II test for accurate mode II fracture toughness determination. The functionality of the MMMB setup was demonstrated by *in-situ* delamination characterization of custom made glued interface structures [26].

2.2. Limitations - Motivation for an improved design

Even though the original MMMB setup was successful in carrying out *in-situ* tests on miniature structures, some limitations persist. First of all, the setup is limited in maximum force (20N) and displacement (depending on the mode mixity) necessary to achieve delamination particularly in mode II and mode II dominant tests. As reported in [26], the clearance in the dovetail connectors may still lead to hysteresis in loading-unloading cycles in the MMMB setup. Using image analysis of the displacements of the dovetail connectors, the influence of the hysteresis could be corrected (only) for mode I tests. Therefore, relatively high error margins may still be expected for mixed mode and mode II measurements. Additionally, some of the hinges in this design are unfavorably loaded in compression, which can lead to hinge failure due to buckling. Finally, the elastic hinges used in the design are fragile, and mounting and un-mounting of the sample demands special care. An improved version of the MMMB device is therefore designed and this design is analyzed, and validated on the CuLF-MCE specimens, as addressed in the next sections.

3. Improved Miniature Mixed Mode Bending setup

The design of the new improved MMMB focused on various fundamental improvements to the original MMMB setup in order to increase its maximum applicable load and stroke limits, to reduce undesirable clearances and to make the setup more robust. Improvements in the design are made by geometry optimization, performed at two structural levels to increase the maximum allowable displacement in the MMMB device. First, the total geometry of the improved MMMB was optimized for maximum global displacement using a finite element beam model of the setup. Next, the geometry of the elastic flexure hinge was optimized to provide more rotation in the critical hinges of the setup. The robustness of the setup was improved by several other modifications to the design including (i) a reversal of all compressive hinges (4 and 5) in the MLM to tensile hinges, (ii) increase in the thickness of the total device, and (iii) incorporation of additional tools for guiding, aligning and securing.

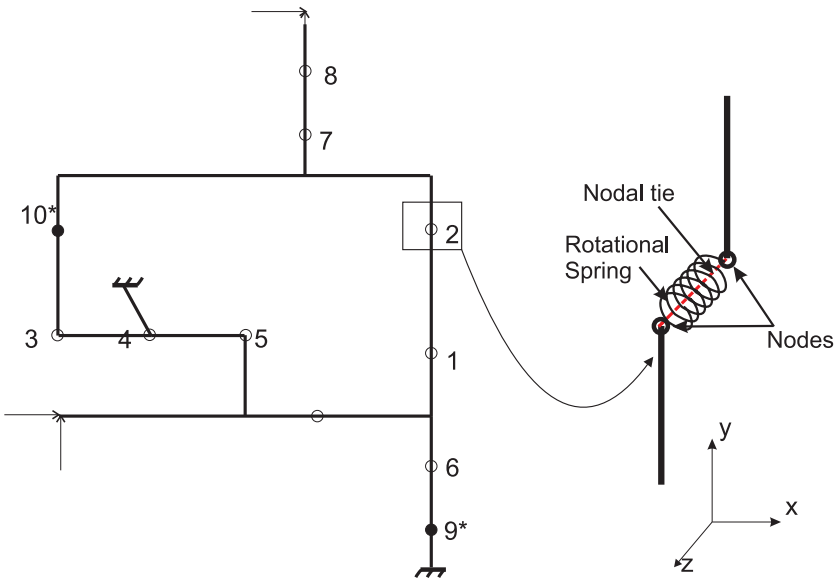

Figure 4. FE beam model of the MMMB setup with new additional hinges. An asterisk '*' indicates the newly added elastic hinges (9 and 10). Details of the nodal ties and hinges are also shown.

3.1. Optimization of the elastic hinge positions

A simple finite element beam model representing the MMMB device shown in figure 4 was used to optimize the geometry of the MMMB device. All the sections of the setup and samples are modeled as simple 2-node beam elements in MSC.Marc. In this model, elastic hinges connecting the beam elements are modeled with nodal ties (with rotation around z-axis being the only untied degrees of freedom) and rotational springs (to incorporate the elastic rotational stiffness and simulate the maximum rotational angle of the elastic hinges), as shown in Fig 4. The hinges in the model are numbered

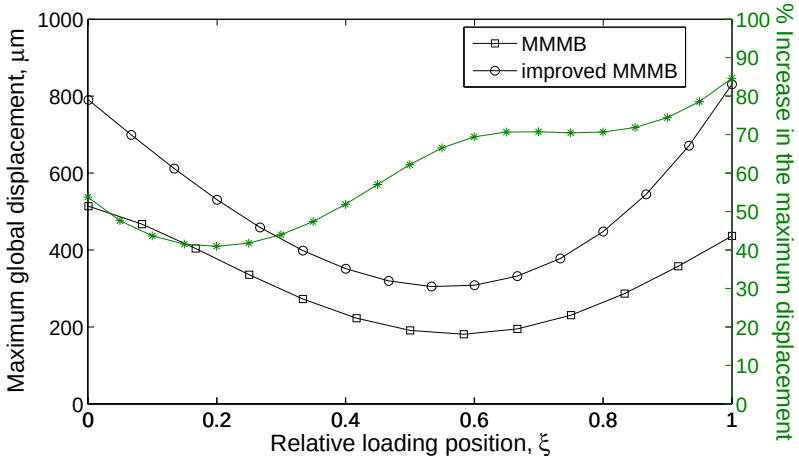

Figure 5. Comparison of the maximum global displacement between the original and improved MMMB configurations, obtained from FE beam simulations performed on a homogeneous bilayer sample with a fixed crack length of 6 mm.

and represented with black circles. A beam model was used because it allows for fast analysis and updates of the position of the hinges and insertion of new hinges. Simulations were performed at all loading positions from $\xi = 0$ to $\xi = 1$ to identify the maximum global displacement at each position and the corresponding critical hinge, i.e. the hinge that reaches its maximum rotation first and therefore limits the maximum global displacement. Hinge 1 appeared to be the critical one in most loading conditions, while mixed mode loading positions close to pure mode II were identified as the critical positions where the global displacements are minimal (Fig. 5). To improve the maximum displacements, two new hinges, one at the right bottom (hinge 9) and one at the left top corner (hinge 10) are inserted in the new design to reduce rotation of critical hinge 1. Figure 6 shows the schematic comparison between the old and new geometries at the same global displacement for a mixed mode test. It is clear from the figure that adding the extra hinges (9, 10) significantly reduces the rotation at hinge 1 (at the expense of increased rotation at hinge 6), which increases the maximum global displacement. From the beam simulations, it became also obvious that more space between hinges 1 and 2 decreases the rotation at hinge 1. In addition, optimization (to maximize distance between hinge 1 and 2) was performed such that the setup uses all the space available ($73 \times 47 \times 29$ mm) in the micro-tensile stage (Kammrath & Weiss GmbH) which is sufficiently small to fit in a scanning electron microscope (SEM) vacuum chamber.

3.2. Optimization of the hinge geometry

After the above-mentioned optimization of the hinge positions, it was concluded that (depending on the loading position) the rotations in hinges 1 or 6 limit the maximum global displacement of the device. Hence, a special elliptic hinge design, which is optimized for an increased maximum rotation, is used to replace the previous circular

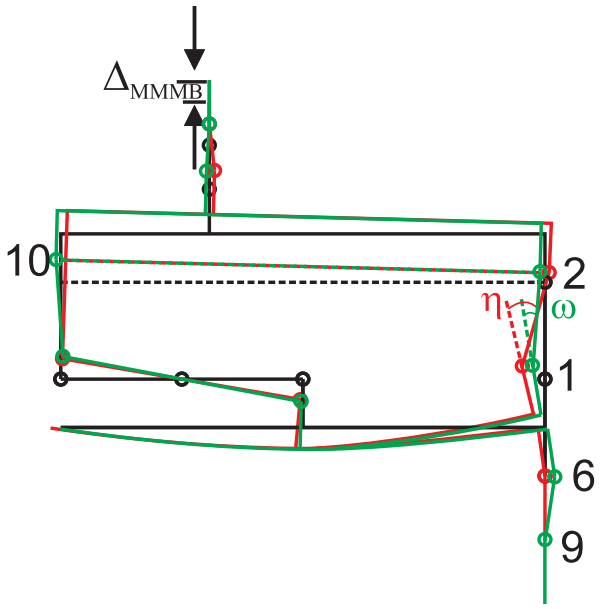

Figure 6. Schematic comparison between the old (red) and new (green) geometries loaded to the same global displacement for a mixed mode test, showing how the introduction of new hinges (9, 10) significantly reduces rotation ($\omega < \eta$) at the critical hinge (no. 1).

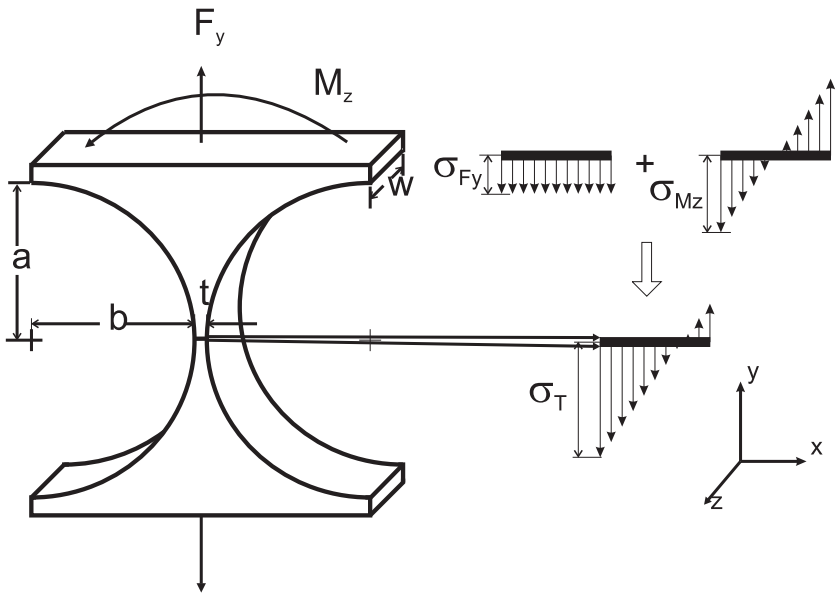

Figure 7. Elliptical flexure hinge with geometrical parameters. The stress distributions across the thickness at t due to the applied moment and the axial force are also shown.

hinges in these critical locations. The other hinges were kept circular because they more accurately preserve the center of rotation than elliptical hinges [28, 29]. Figure 7 shows the parameters representing the geometry of the hinge. The maximum rotation of a

hinge is determined by the geometry parameters (b/a ratio) that define the profile of the hinge, width w and the thickness t at the thinnest region of the elastic hinge. The thinnest hinge region with thickness t carries the bending stress, σ_{M_z}, and normal stress, σ_{F_y}, that can be applied to the hinge. Optimization of this thickness is done using the closed form compliance equation derived by Smith et al., [30] for elliptic hinges:

$$M_z = \frac{\theta_z E w t^3}{24 a \gamma}, \tag{5}$$

where γ is a lengthy function of b and t. The maximum total stress (σ_T), which is at the surface, is the sum of the stress contribution from the applied moment around the z-axis ($\sigma_{M_z} = K_t \frac{M_z.t}{2I_{zz}}$, where K_t the stress concentration factor is a function of a and t, and where I_{zz} is the moment of inertia at t) and the applied normal stress along the x-axis ($\sigma_{F_y} = \frac{F_y}{tw}$). For a hinge in an elastic state, σ_T should remain below the yield strength σ_Y of the material, reduced with a safety factor ζ, i.e.

$$\sigma_{M_z} + \sigma_{F_y} \leq \frac{\sigma_Y}{1+\zeta}. \tag{6}$$

The maximum rotation of the hinge can be retrieved by rearranging equations (5) and (6) as,

$$\theta_z = \left[\frac{\sigma_Y}{1+\zeta} - \frac{F_y}{tw}\right] \frac{48 a I_{zz}}{K_t E w t^4} \gamma(b,t). \tag{7}$$

θ_z in equation (7) can be treated as the objective function to maximize, leading to an optimal geometry of the hinge (t, w, a and b). From Eq. 7, it is obvious that θ_z increases monotonically with increasing hinge length, a, however, this is counteracted by a decrease in the precision of the rotation. Hence, the hinge profile ($\frac{b}{a} = 0.8626$) suggested by Chen et al., [28] for optimal hinge performance with respect to maximum rotation at minimal stress concentration and maximum precision of rotation was used here. In addition, the width w was increased (from 2 mm in the original setup) to 6 mm in order to increase the allowable maximum axial force F_y from 20 N to 50 N. The other constraint is $b \leq 3.25$ mm which is limited by the available space in the tensile stage. Using $b = 3.25$ mm, θ_z is plotted as a function of the thickness for an elliptic hinge in Fig. 8. A maximum rotation angle θ_{zmax} of 8.62° is found (without any safety factor) for $t = 28$ μm as shown in Fig. 8. With a safety factor of $\zeta = 0.2$, the maximum rotation angle is reduced to $\theta_{zmax} = 6.56°$ for $t = 34$ μm. Based on the limited sensitivity to t around the maximum (Fig. 8), a value of $t = 50$ μm was adopted for the final design to avoid the region of high sensitivity of θ_{zmax} to possible machining inaccuracies for small thicknesses. This slightly reduces the maximum rotation angle to 6.27°. In all, the maximum rotation has improved with 32% compared to the hinges in the original design, using the same safety factor. Moreover, the extent of the profile of the hinge on one side was reduced to the minimum distance ($y = \frac{x}{2}$) without influencing the maximum rotation of the hinge [29], in order to maximize the distance between hinge 1 and 2 (Fig. 4).

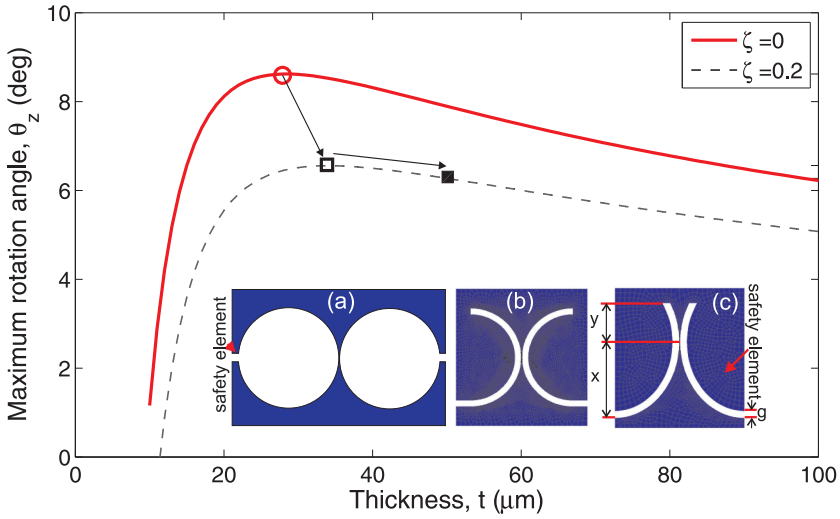

Figure 8. Maximum rotational angle θ_z as a function of the thickness t of the hinge for $w = 6$ mm, $b = 3.25$ mm and $\frac{b}{a} = 0.8626$. Inset: (a) a conventional elastic hinge, (b) the circular hinge used in the original MMMB setup and (c) the new elliptic hinge design with a reduced profile on one side. The safety element closes the safety groove, g, once the hinge rotates to the maximum allowable rotational angle.

3.3. Final improved MMMB design

Incorporating the above mentioned modifications, FE beam simulations were performed with the improved MMMB design to check its performance. The maximum global displacement was plotted as a function of the relative loading position in Fig. 5, which is improved by more than 60% for the critical loading positions close to pure mode II. Then, the improved MMMB device was manufactured by electrical discharge machining of the Ti-6Al-4V alloy plate. The final design of the improved MMMB device in comparison with the original MMMB device is shown in Fig. 9. All the important changes are highlighted and numbered. It is also noted that the improved design has 16 mode selector positions, instead of 13, in order to more accurately select the mode angle in the experiment. The main parts of the improved MMMB setup mounted in the micro-tensile stage are depicted in Fig. 10. Besides the above mentioned improvements in maximum load and displacement, also the remaining nonlinearities and robustness were further addressed, which is discussed next.

3.4. Clearance and Robustness of the setup

As was reported in [26], the clearance in the dovetail connectors resulted in hysteresis in the load displacement curves during loading-unloading tests in the original MMMB setup. The hysteresis can only be corrected for in mode I tests by tracking the connector clearance using a digital image correlation technique [31], a correction that is not possible in mixed mode and mode II measurements. To overcome this problem, new tapered dovetail connectors with wedge locking tools were manufactured as shown in Fig. 10b.

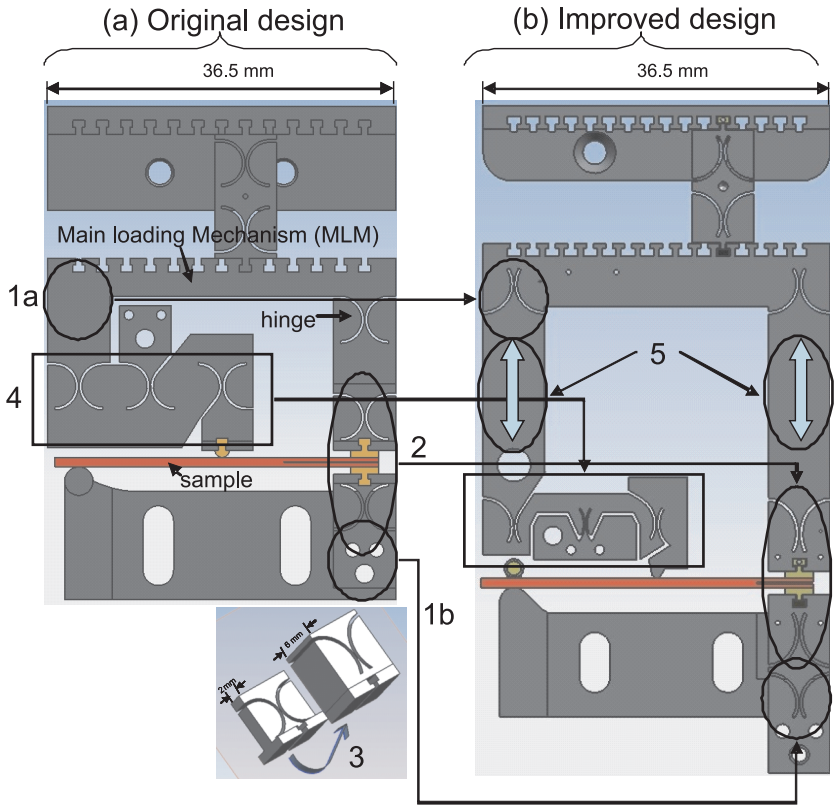

Figure 9. Design of (a) the original and (b) the improved MMMB setup. Improvements are highlighted and numbered: (1) introduction of new hinges, (2) replacement of the critical hinges with elliptical hinges for increased rotation, (3) optimization of hinge geometry and increased robustness, (4) redesign of compressive hinges to tensile loading, and (5) increased length of the MLM.

With these tapered dovetails, mounting of the sample becomes easy and requires a relatively small force (in contrast to the original setup) which avoids any deformation of the hinges in the setup. After mounting the sample into the setup, the wedge tools are inserted to lock the dovetails without any clearance.

Since the elastic hinges used in the design are fragile, any damage of the hinge due to small forces during insertion and removal of the sample and the wedge locking tools and during actual loading should be avoided. Hence the following features have been adapted.

(i) The thickness of the device is increased from 2 to 6 mm

(ii) The hinges at the mid loading position (hinge no. 4 and 5) are designed to be under tension to avoid any buckling of the hinges due to compressive loading in mode II dominated tests.

(iii) A separate bottom hinge shown in Fig. 10 (as 2b) is used when the load at this hinge is compressive ($P_D < 0$) to avoid an unstable bottom hinge configuration.

(iv) Several components including guiding pins (to prevent in-plane motion) as well as

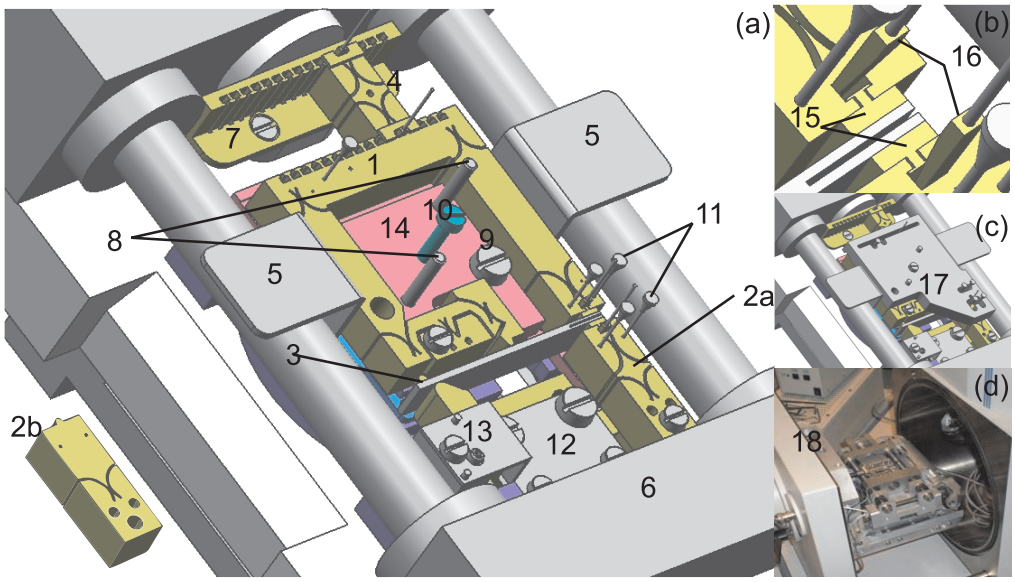

Figure 10. (a) the improved MMMB setup mounted in the micro-tensile stage: (1) main loading mechanism, (2a,2b) bottom hinges, (3) sample, (4) position selector, (5) handling plate, (6) micro-tensile stage, (7) position bar, (8) guiding rods, (9) set screw, (10) screw lock, (11) alignment pins, (12) sample height adjuster, (13) alignment screw, (14) bottom plate. (b): (15) new tapered dovetail connectors and, (16) wedge locking tools that remove any clearance in the connectors. (c): (17) top supporting plate (to lock the device during insertion and removal of the wedges) and (d): improved MMMB setup mounted in (18) SEM chamber.

a top and (movable) bottom supporting plate (to prevent out of plane motion) were introduced to provide mechanical isolation of the hinges and highly accurate alignment of the MLM during sample insertion and removal.

All these features significantly increase the robustness of the setup. Additionally, using these locking tools, the interface to be tested will also be protected from any external loads during the mounting process. In conclusion, the new robust setup increases the precision of the experimental load-displacement measurement by minimizing the risk for handling errors.

4. Analysis of the new improved MMMB setup

4.1. Validation and accuracy assessment

The performance of the improved MMMB setup is evaluated using specially designed validation samples to assess the influence from inaccuracies in the manufactured geometry, machine compliance, or other factors such as clearance at the connectors. These samples are homogeneous single layer brass samples (i.e. without an interface and hence no propagating crack) with a well-defined notch, having an opening width of 30 μm, representing an existing crack of fixed length. The thickness of these samples is 1

mm. The inset in Fig. 11a shows the extremity with the notch in one of the test samples. Test samples with 5 different notch lengths (3, 6, 9, 12 and 15 mm) were used to check the performance of the setup. Tests were performed at all loading positions from mode I to pure mode II ($\xi = 0 - 0.8$). Figure 11a shows the results of these tests performed on the 12 mm notch sample. The hysteresis observed in these tests is negligibly small, confirming the efficacy of the new wedge-locking dovetails with minimal clearance at the connectors (Fig. 10b). The relative hysteresis, defined as the dissipated energy during a loading-unloading cycle, relative to the energy supplied during loading was calculated for all crack lengths and different loading positions. The maximum relative hysteresis was found to be 2% for pure mode II and the mean value is 1% for all loading positions. This is at least a factor of 2 smaller compared to the original design [26], even without the need for an elaborate digital image correlation correction procedure. To assess the precision of the complete experimental procedure, repeated tests were performed at one loading position by unmounting the sample after each test and remounting it for the next test. Because of the increased robustness and the new alignment tools, consistent results can be obtained (Fig. 11b). Specifically, the error in the stiffness was less than 0.7% which demonstrates the achieved precision of the new design.

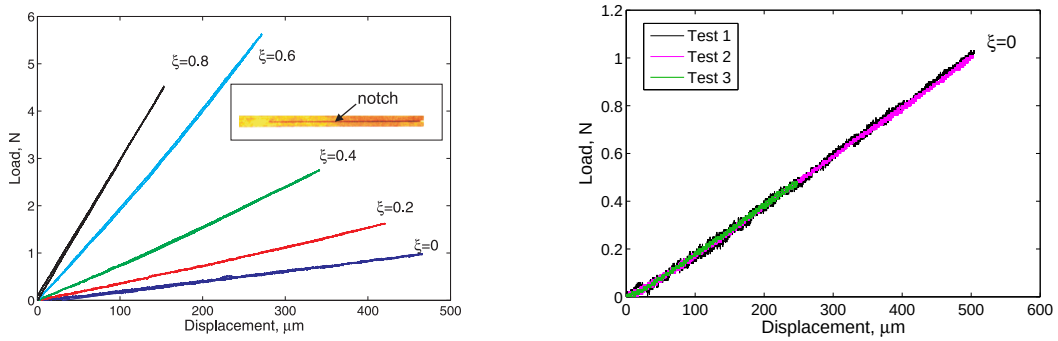

Figure 11. (a) Load-displacement results for loading-unloading cycles with the 12 mm validation sample at different loading positions (indicated by ξ). The inset shows the notched extremity of a validation sample used for mode I to pure mode II tests $\xi = 0 - 0.8$. (b) Results of complete experimental repetition of 3 validation tests performed at $\xi = 0$. An error of less than 0.7% in stiffness was observed.

4.2. Finite Element Analysis

To determine the mode angle at the interface for different relative loading positions, finite element (FEM) simulations were performed for all loading positions using the beam model of the setup and an elastic material model of the CuLF-MCE sample. A fixed length of the precrack was modeled with a special rosette shape crack tip mesh. The mode angle, ψ, is defined by the orientation of the stress field. Because of the oscillating stress field in the dissimilar material interface (CuLF-MCE interface) [13], ψ

is defined at a certain reference length, δ:

$$\psi = \arctan\left(\frac{\sigma_{12}}{\sigma_{22}}\right)_{\delta}, \tag{8}$$

where σ_{22} is the normal stress, σ_{12} is the shear stress. The plastic process zone size is a common choice for the reference length δ [13, 14] as it is the only intrinsic length scale in the system. The size of this process zone can be defined by the point where the linear elastic stress field equals the yield stress of the weakest of the two materials [13], which is 5 μm in case of the CuLF-MCE samples. The mode angles calculated from the FEM simulations are plotted as a function of loading position in Fig. 12. The figure also shows this relation for a homogeneous bilayer sample with equal thickness of the bulk layers. These calculations demonstrate that the setup probes interface delamination over the complete range of mode angles for both homogeneous and dissimilar bilayer samples. Additionally, a strong feature of the MMMB concept is that the mode angle stays constant within a few degrees for different crack lengths and MLM displacements, as was shown previously [26]. It is also worth mentioning that FEM simulations taking into account the actual geometry of the setup, showed that at a maximum load of 50N, the displacement resulting from the compliance of the MMMB setup can be neglected with respect to the measured global displacement.

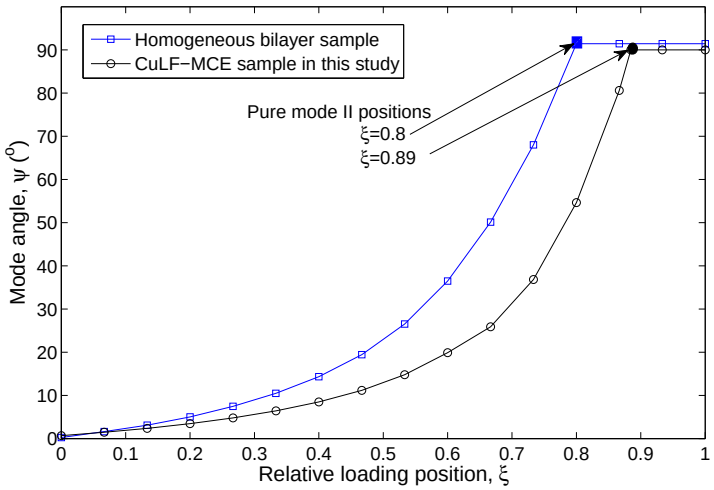

Figure 12. Mode angle obtained by FEM analysis as a function of relative loading position (ξ) for (i) a homogeneous equal thickness bilayer sample and (ii) the CuLF-MCE sample used in this study, with a crack length of 6 mm at 200 μm MLM displacement.

5. Study of coated copper lead frame - molding compound epoxy (CuLF-MCE)

5.1. Experimental procedure

In-situ experiments with the improved MMMB setup were conducted in a scanning electron microscope and under an optical stereo microscope at high magnifications. A batch of bilayer samples (manufactured at Philips Applied Technologies), consisting of 0.2 mm thick preplated (Au-Pd-Ni) copper lead frame and 0.5 mm thick molding compound epoxy, was tested in these experiments. The samples were prepared by heating the lead frame to 180°C for 2.5 minutes followed by high pressure hot injection molding of the molding compound epoxy. Afterwards, the samples were laser cut to the required dimensions (35 × 5 mm). After the molding, the samples received a post mold cure for 4 hours at 175°C. At the end of each sample, a well defined 6 mm long pre-crack was created by sliding a thin knife edge between the two layers using a home-built device. Prior to the experiment, samples were fine polished on one side (perpendicular to the plane of the interface) to visualize the interface at high magnifications. The dovetail connectors were attached on both sides of the samples with a stiff glue at the pre-cracked end, after which the samples were carefully mounted into the setup, by applying the robust sample insertion procedure with locked elastic hinges, as explained in section 3.4. Finally, the position selector was reinserted at the appropriate position to carry out a delamination experiment at the desired mode angle. During the test, the sample was unloaded and reloaded at regular intervals. At each load reversal, images of the crack tip were recorded at a magnification of 250x. These images were used to determine the crack length corresponding to the load reversals in the post processing analysis. On the basis of these experiments, the interface properties of the preplated CuLF-MCE interface structure were characterized over a complete range of mode mixities, thereby demonstrating the strengths of the setup.

5.2. Results and discussion

Figure 13 shows the load-displacement plots of the *in-situ* experiments conducted under a stereo microscope, at mode I ($\xi = 0$) and mixed mode loading positions ($\xi = 0.4$, 0.67 and 0.8). Initially, in all mode mixities, the load increases linearly with increasing displacement until the onset of crack initiation. Subsequently, a gradual drop in the load is observed with further displacement due to crack propagation. It is observed that the maximum at the onset of crack initiation in the first loading-unloading cycle is less pronounced compared to the sharp maximum observed in the subsequent cycles, as highlighted in red in Fig. 13 for the mode I curve. This smooth behavior in the first cycle is attributed to the gradual development of a sharp microscopic crack tip and stable crack front normal to the crack propagation direction. Hence, before the actual delamination experiment at certain mode mixity, each sample was first loaded in mode I (position $\xi = 0$), until the initiation of a sharp stable crack front was established. This

first mode I cycle was ignored for the calculation of the CERR and is also not shown for the mixed mode experiments in Fig. 13.

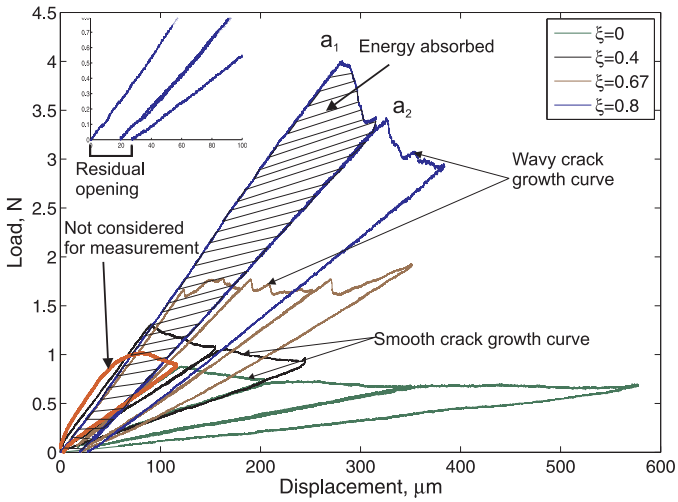

Figure 13. Comparison of load-displacement plots of a mode I ($\xi = 0$) and mixed mode ($\xi = 0.4, 0.67, 0.8$) experiments conducted on CuLF-MCE samples. The inset shows a magnification around the origin of the $\xi = 0.8$ curve illustrating the residual opening after unloading to zero load.

The critical energy release rate of the interface was calculated from the area between the successive loading-unloading stiffness lines (e.g. the hashed region in Fig.13), divided by the delaminated area corresponding to an increase of the crack length from position a_1 to a_2. A strong feature of the (improved) MMMB setup is that it allows highly accurate determination of the crack tip position under the SEM, therefore, there is no need to use approximate analytical formula or numerical tools for the crack length prediction to calculate the CERR values. The resulting CERR values are shown in Fig. 14 as a function of the mode angle (the latter is determined from FE simulations). Note that the CERR measured represents the macroscopic interfacial fracture energy, which may include contributions from other dissipative mechanisms like plasticity in the layers and/or at the interface. This is particularly the case when a ductile layer is present in the composite stack [32, 33]. For instance, the inset in Fig. 13 shows a zoom around the origin of the load-displacement plot for $\xi = 0.8$, revealing a residual opening after complete unloading indicating plasticity contributions to the measured CERR. Identification of the individual contributions of plasticity, e.g. to eliminate bulk plasticity from the calculation of CERR, requires a dedicated numerical-experimental methodology which is beyond the scope of this paper. For the present work, the maximum contribution to the measured CERR value due to bulk plasticity has been estimated from Fig. 13 by assuming a full damage unloading behavior to the origin. A maximum deviation of 6% about the mean CERR value was observed in mode II dominant test at $\xi = 0.89$, while a negligible influence was observed in mode I or mode

I dominant mixed mode tests.

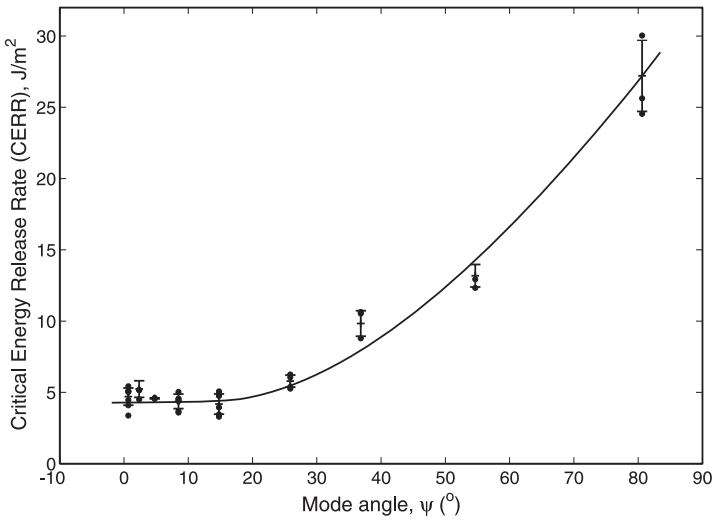

Figure 14. Critical energy release rate with standard deviation bandwidth as a function of mode angle.

Besides the energy absorbed between two successive loading-unloading cycles, other important details are visible in Fig. 13. The first important observation is that the hysteresis of the setup, which can be measured from the unloading-reloading curves is negligible in all of the tests (even better than Fig. 11(a)). It is also clear that the curves (during crack growth) are smooth for mode I dominant tests (at $\xi = 0$ and 0.4) compared to the wavy curves in mode II dominant tests ($\xi = 0.67$, 0.8). This difference in behavior can be attributed to the roughness of the bonded surfaces (which is $\sim$1 μm RMS for the copper layer before molding) at the interface. Locally, the micro-scale roughness can lead to local shearing of and/or sliding between roughness asperities causing additional frictional dissipation which leads to an increased macroscopic interface fracture energy. In both cases, apart from the bulk layers that need to store more energy, a local crack opening displacement on the order of the roughness or size of the asperities is necessary for the crack to grow. In shear dominant tests (e.g. pure mode II), where the crack opening in normal direction is constrained, individual asperities will need to shear for the crack to grow. Therefore, either frictional sliding or local shearing can explain the discrete crack growth with its resulting characteristic wavy behavior for mode II dominant curves. To substantiate this hypothesis, *in-situ* delamination tests under SEM at high magnifications were carried out, confirming that the crack grows smoothly in mode I dominant tests (ξ = 0-0.53), compared to more discrete or jerky crack growth in mode II dominant tests (ξ = 0.53-1). This is also consistent with the trend in the CERR in Fig. 14, where a CERR of $\sim$ 4.5 J/m^2 that is constant within experimental uncertainty was observed until $\psi \approx 15^\circ$ (i.e. ξ = 0-0.53), followed by a sharp increase with increasing mode angle towards position $\xi = 1$.

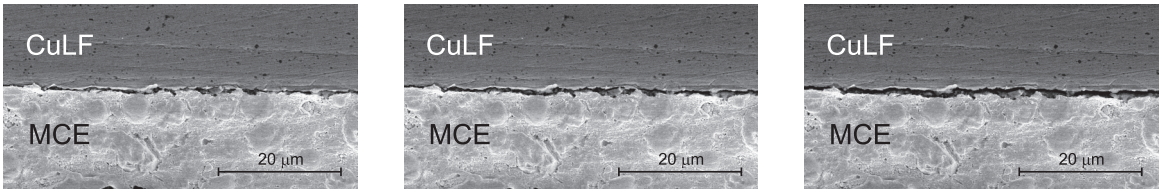

(a) (b) (c)

Figure 15. SEM micrographs showing the evolution of crack (from a-c) in the process zone during delamination. The crack is growing from the right to left.

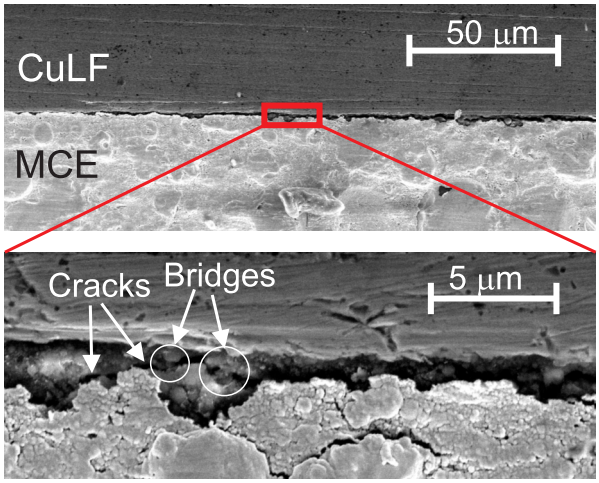

Figure 16. SEM micrograph showing small cracks and a limited number of bridges at the interfaces.

In addition to the CERR measurements, real-time microscopic visualization allowed extraction of additional information at the delamination front to trace the formation and propagation of the crack in detail, providing valuable input for understanding of the fracture mechanism and for predictive simulations of the delamination in these interfaces. Specifically, the microscopic images allow for the following measurements.

(i) The precise crack tip position can be determined within an accuracy of 5 μm.

(ii) The delamination mechanism can be visualized at the interface. Figure 15 shows the evolution of the crack in the process zone. A brittle cleavage type of failure was observed as the dominant mechanism indicating the brittle nature of the interface. At high magnifications, some bridges were observed as shown in Fig. 16.

(iii) The displacement field during delamination can be mapped using a digital image correlation (DIC) technique. As a first demonstration of resolving local strain fields, a DIC generated y-displacement field around the crack tip is shown in Fig. 17. By measuring the evolution of the full profile of the crack opening during initiation of the delamination crack, important local information such as the elongation of the interface (glue) layer at the crack tip, and the rotation of the loading point can be extracted, which can be used in combination with the measured applied load and

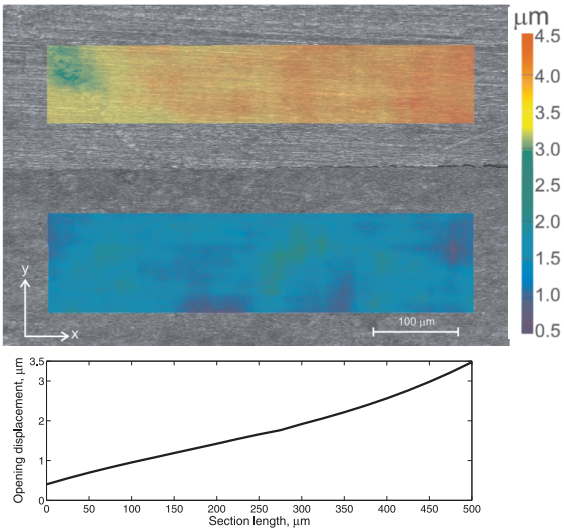

Figure 17. SEM micrograph with a DIC overlay of the y-displacement at a certain opening. Opening displacement as a function of section length is shown in the graph below.

the sample width to calculate the full interface traction-separation law using the approach proposed by Andersson et al. [34].

6. Conclusions

An improved miniature mixed mode bending setup capable of *in-situ* delamination testing in advanced microscope systems (e.g. scanning electron microscope) has been proposed, designed, manufactured and tested. Improvements in the present design are: (i) optimal number and location of the hinges, (ii) optimal elastic hinge geometries for increased maximum rotation and (iii) minimized clearance at the connectors and increasing robustness of the setup with additional guiding and alignment tools. It was demonstrated that the improved setup exhibits

(i) a wider application range to more interface systems because of its significant increase of the maximum accessible load and stroke in all mode mixities,

(ii) good accuracy in measuring the load-displacement response, as demonstrated from experiments on validation samples, confirming the significantly reduced hysteresis,

(iii) excellent experimental reproducibility characteristics due to the newly added alignment tools.

The improved setup was used for testing industrially relevant CuLF-MCE samples in the full range of mode mixities. Unloading-reloading tests performed at different mode mixities were used to calculate the CERR. In addition to the CERR measurements, real-time microscopic visualization allowed the identification of the difference in the crack growth behavior between different mode mixity tests. At small mode angles ($\psi < 15°$)

relatively smooth crack growth behavior was observed resulting in a constant CERR value of ~ 4.5 J/m^2. At mode angles greater than 15°, however, a jerky crack growth was observed with a serrated load-displacement response, which suggest its direct correlation with the observed increase in CERR with increasing mode angle from 15° to 90°. In-situ visualization also allowed to determine the precise position of the crack tip, and the crack opening displacement using DIC technique, as well as a qualitative assessment of the active delamination mechanism at the interface. A brittle cleavage failure type was observed for the investigated CuLF-MCE samples, while at high magnifications, some crack bridges were also observed.

Acknowledgements This research was carried out under the project number MC2.05235 in the framework of the research program of the Materials Innovation Institute M2i (www.m2i.nl). The authors are grateful to Marc van Maris for his assistance in conducting some of the reported experiments and Lisanne Dautzenberg for her contributions to the FE simulations. Peter Timmermans and Olaf van der Sluis from Philips are acknowledged for their help in manufacturing and supply of samples.

Appendix

Expressions for the mode I (Eq. 2), mode II (Eq. 3) and relative loading position for pure mode II (Eq. 4) are derived here. From Fig. 3, the force and moment balances directly yields Eq. 3,

$$P_{II} = P_B = P_{\mathrm{MMMB}}\frac{\alpha}{\beta}\xi. \tag{3}$$

Other balance equations are,

$$P_A = P_I + P_E \tag{A.1}$$

$$P_E + P_F = \frac{P_{II}}{2}. \tag{A.2}$$

Combining $K = \frac{P_E}{P_F}$ with Eq. A.2 gives,

$$P_F = \frac{P_{II}}{2(1+K)} \tag{A.3}$$

$$P_E = K\frac{P_{II}}{2(1+K)}. \tag{A.4}$$

Substituting Eqs. 1a and A.4 in Eq. A.1, results in,

$$P_I = P_{\mathrm{MMMB}}(1-\xi) - K\frac{P_{II}}{2(1+K)}. \tag{A.5}$$

Furthermore, substituting Eq. 3 in Eq. A.5 yields,

$$P_I = P_{\mathrm{MMMB}}\left(1 - \xi - \frac{K\alpha}{2\beta(1+K)}\xi\right), \tag{2}$$

which is the equation for mode I component (Eq. 2). For pure mode II loading, substituting $P_I = 0$ in Eq. 2 and solving for ξ yields Eq. 4:

$$\xi_{II} = \frac{2(1+K)\beta}{K\alpha + 2(1+K)\beta}. \tag{4}$$

References

[1] O. van der Sluis, R. A. B. Engelen, R. B. R. van Silfhout, W. D. van Driel, and M. A. J. van Gils. Efficient damage sensitivity analysis of advanced Cu/low-k bond pad structures by means of the area release energy criterion. *Microelectronics Reliability*, 47:1975–1982, 2007.

[2] W. D. van Driel, M. A. J. van Gils, R. B. R. van Silfhout, and G. Q. Zhang. Prediction of delamination related IC and packaging reliability problems. *Microelectronics Reliability*, 45:1633–1638, 2005.

[3] H. Y. Lee and G. S. Park. Failure paths at copper-base leadframe/epoxy molding compound interfaces. *Journal of Materials Science*, 37:4247–4257, 2002.

[4] N. Tanaka, M. Kitano, T. Kumazawa, and A. Nishimura. Evaluating IC-package interface delamination by considering moisture-induced molding-compound swelling. *IEEE Transactions on Components and Packaging Technology*, 22(3):426–432, 1999.

[5] F. M. Pan, S. R. Horng, T. D. Yang, and V. Tang. Studies of the interface between the epoxy molding compound and the copper leadframe by X-ray photoelectron spectroscopy, auger electron spectroscopy, and secondary electron spectroscopy. *Journal of Vacuum Science and Technology A*, A(6):4074–4078, 1990.

[6] L. Xu, X. Lu, J. Liu, X. Du, Y. Zhang, and Z. Cheng. Adhesion behavior between epoxy molding compound and different leadframes in plastic packaging. *Proceedings of International Conference on Electronic Packaging Technology and High Density Packaging (ICEPT-HDP)*, pages 1039–1042, 2009.

[7] A. Xiao, L. G. Wang, W. D. van Driel, L. J. Ernst, 0. van der Sluis, D. G. Yang, and G. Q. Zhang. Characterization and modeling of thin film interface strength considering mode mixity. *In IEEE Transactions of Electronic Components and Technology Conference*, ISBN 1-4244-0985-3:1925–1930, 2007.

[8] N. Srikanth, L. Chan, and C. J. Vath-III. Adhesion improvement of EMC-leadframe interface using brown oxide promoters. *Thin Solid Films*, 504:397–400, 2006.

[9] J. Thijsse, O. van der Sluis, J. A. W. van Dommelen, W. D. van Driel, and M. G. D. Geers. Characterization of semiconductor interfaces using a modified mixed mode bending apparatus. *Microelectronics Reliability*, 48:401–407, 2008.

[10] B. A. E. van Hal, R. H. J. Peerlings, M. G. D. Geers, and O. van der Sluis. Cohesive zone modeling for structural integrity analysis of IC interconnects. *Microelectronics Reliability*, 47:1251–1261, 2007.

[11] M. J. van den Bosch, P. J. G. Schreurs, and M.G.D. Geers. An improved description of the exponential Xu and Needleman cohesive zone law for mixed-mode decohesion. *Engineering Fracture Mechanics*, 73:1220–1234, 2006.

[12] R. Borg, L. Nilsson, and K. Simonsson. Simulating DCB, ENF and MMB experiments using shell elements and a cohesive zone model. *Composite Science and Technology*, 64:269–278, 2004.

[13] J. W. Hutchinson and Z. Suo. Mixed mode cracking in layered materials. *Advances in Applied Mechanics*, 29:63–191, 1992.

[14] Z. Suo and J. W. Hutchinson. Interface crack between two elastic layers. *International Journal of Fracture*, 43:1–18, 1990.

[15] K. M. Liechti and Y. S. Chai. Asymmetric shielding in interfacial fracture under in-plane shear. *Journal of Applied Mechanics*, 59:295–304, 1992.

[16] W. O. Soboyejo, G. Y. Lu, S. Chengalva, J. Zhang, and V. Kenner. A modified mixed-mode bending specimen for the interfacial fracture testing of dissimilar materials. *Fatigue and Fracture of Engineering Materials and Structures*, 22:799–810, 1999.

[17] L. Banks-Sills, Nahum Travitzky, and Dana Ashkenazi. Interface fracture properties of a bimaterial ceramic composite. *Mechanics of Materials*, 32:711–722, 2000.

[18] X. Q. Shi, X. R. Zhang, and J. H. L. Pang. Determination of interface fracture toughness of the adhesive joint subjected to mixed-mode loading using finite element method. *International*

Journal of Adhesion and Adhesives, 26:249–260, 2006.

[19] R. Rikards, F. G. Buchholz, H. Wang, A. K. Bledzki, A. Korjakin, and H. A. Richard. Investigation of mixed mode I/II interlaminar fracture toughness of the laminated composites by using a CTS type specimen. *Engineering Fracture Mechanics*, 61:325–342, 1998.

[20] J. R. Reeder and J. R. Crews. Mixed mode bending method for delamination testing. *AiAA Journal*, 28(7):1270–1276, 1990.

[21] G. Wang, C. Merrill, J-H Zhao, and S. K. Groothuis. Packaging effects on reliability of cu/low-k interconnects. *IEEE Transactions on Device and Materials Reliability*, 3(4):119–128, 2003.

[22] C. C. Merrill and P. S. Ho. Effect of mode mixity and porosity on interface fracture of low-k dielectrics. In *Materials Research Society Symposium Proceedings*, volume 812, 2004.

[23] N. Blanco, E. K. Gamstedt, J. Costa, and D. Trias. Analysis of the mixed-mode end load split delamination test. *Composite Structures*, 76:14–20, 2006.

[24] G. V. Marannano and A. Pasta. An analysis of interface delamination mechanisms in orthotropic and hybrid fiber-metal composite laminates. *Engineering Fracture Mechanics*, 74:612–626, 2007.

[25] R. T. Tenchev and B. G. Falzon. A correction to the analytical solution of the mixed-mode bending (mmb) problem. *Composite Science and Technology*, 67:662–668, 2007.

[26] M. Kolluri, M. H. L. Thissen, J. P. M. Hoefnagels, J. A. W. van Dommelen, and M. G. D. Geers. *In-situ* characterization of interface delamination by a new miniature mixed mode bending setup. *International Journal of Fracture*, 158:183–195, 2009.

[27] ASTM-D-6671-01. *Standard test method for mixed mode I-mode II interlaminar fracture toughness of unidirectional fiber reinforced polymer matrix composites, Annual book of ASTM standards*, volume 15.03. American Society for Testing and Materials, West Conshohocken, PA., 2001.

[28] G. Chen, J. Jia, and Q. Han. Geometrical profile optimization of elliptical flexure hinge using a modified particle swarm algorithm. *ICIC 2005, part I, LNCS 3644*, page 533 542, 2005.

[29] G. Chen, X. Shao, and X. Huang. A new generalized model for elliptical arc flexure hinges. *Review of Scientific Instruments*, 79(095103):1 8, 2008.

[30] S. T. Smith, V. G. Badami, J. S. Dale, and Y. Xua. Elliptical flexure hinges. *Rev. Sci. Instrum.*, 68(3):1474–1483, 1997.

[31] M. Kolluri, M. H. L. Thissen, J. P. M. Hoefnagels, J. A. W. van Dommelen, and M. G. D. Geers. Study of interface delamination by a newly designed miniature mixed mode bending setup. In *Proceedings of European conference on fracture (ECF) 17, CD-ROM*, 2008.

[32] M. Lane, R. H. Dauskardt, A. Vainchtein, and H. Gao. Plasticity contributions to interface adhesion in thin-film interconnect structures. *Journal of Material Research*, 15(12):2758–2769, 2000.

[33] S. Strohband and R. H. Dauskardt. Interface separation in residually-stressed thin-film structures. *Interface Science*, 11:309–317, 2003.

[34] T. Andersson and U. Stigh. The stress-elongation relation for an adhesive layer loaded in peel using quilibrium of energetic forces. *International Journal of Solids and Structures*, 41:413434, 2004.